

Low-cost and large-scale synthesis of functional porous materials for phosphate removal with high performance†

Cite this: *Nanoscale*, 2013, 5, 6173

Irene Emmanuelawati,‡ Jie Yang,‡ Jun Zhang, Hongwei Zhang, Liang Zhou* and Chengzhong Yu*

A facile spray drying technique has been developed for large-scale and template-free production of nanoporous silica with controlled morphology, large pore size, and high pore volume, using commercially available fumed silica, Aerosil 200, as a sole precursor. This approach can be applied to the preparation of functional nanoporous materials, in this study, lanthanum oxide functionalised silica microspheres by introducing lanthanum nitrate *in situ* during the spray drying process and followed by a post-calcination process. The resultant lanthanum functionalised Aerosil microspheres manifest high phosphate adsorption capacity (up to 2.317 mmol g⁻¹), fast kinetics, and excellent adsorption performance at a low phosphate concentration (1 mg L⁻¹). In virtue of the easy and scalable synthesis method, low cost and high performances of the product, the materials we reported here are promising for water treatment. Our approach may be general and extended to the synthesis of other functional nanoporous materials with versatile applications.

Received 30th March 2013

Accepted 3rd May 2013

DOI: 10.1039/c3nr01574b

www.rsc.org/nanoscale

Introduction

Porous materials with large surface area, high pore volume, and tunable pore size are of great scientific and industrial interest due to their diverse applications in catalysis, adsorption, and separation.¹ Various methods for producing mesoporous and macroporous materials have been established, which are generally based on templating approaches.^{2–6} The employment of templates, such as surfactants,^{2–4} emulsions,⁵ and colloidal crystals,⁶ raises the costs of products to a large extent, thus limiting the commercial viability of the resultant porous materials. In this regard, a cheap and facile approach for the large-scale synthesis of porous materials, particularly functional porous materials, is highly desirable. Besides templating, it has been reported recently that periodic packing of monodispersed silica spheres can also give rise to uniform interstitial mesopores.^{7,8} It has long been known that spray drying can be utilized to assemble silica colloids into microspherical particles.^{9–11} These accomplishments have inspired us to spray dry commercialized silica nanoparticles in preparing porous silica materials.

Eutrophication, caused by the accumulation of excessive nutrients such as phosphorous (P) and nitrogen (N) species in water bodies, has become a big threat around the world.¹² It may lead to algal blooms, fish kills, “dead zones”, and, eventually, ecosystem collapse. To mitigate eutrophication, it is critical to decrease the P inputs and/or the P concentration in water bodies.^{13,14} P exists almost solely as phosphates, which can be further classified into orthophosphates, polyphosphates, and organically bound phosphates. Various techniques, such as chemical precipitation, biological treatment, and adsorption, have been proposed for phosphate removal. Chemical precipitation with Fe, Al and Ca components, although widely used in treating industrial effluents, produces a large volume of sludge, the dispose of which is a problem.¹⁵ The biological removal is usually non-specific, the disposal of sludges containing condensed phosphates, heavy metals, and microorganisms also causes environmental risks and safety concerns.¹⁵ Moreover, it is technically difficult for both techniques to remove phosphates to levels that can satisfy the stringent regulations.¹⁶

Adsorption is another method and very promising for phosphate removal due to less sludge production, effectiveness at low phosphate concentrations, and the possibility for phosphate recovery. Among the various adsorbents developed for phosphate removal, functional nanoporous materials are particularly attractive.^{17–20} Shin and co-workers found that Al impregnated SBA-15 was a promising adsorbent for phosphate removal.¹⁷ Ou *et al.* synthesized lanthanum doped MCM-41 by a sol-gel process and found that the phosphate removal capacity

Australian Institute for Bioengineering and Nanotechnology, The University of Queensland, Brisbane, QLD 4072, Australia. E-mail: lzhou1@uq.edu.au; c.yu@uq.edu.au; Fax: +61 7-334-63973; Tel: +61 7-334-63283

† Electronic supplementary information (ESI) available: EDX results of La₃-A; XRD pattern of La(NO₃)₃·6H₂O after calcination in air at 550 °C for 5 h; and XRD pattern of La₁₅₀-A after phosphate adsorption. See DOI: 10.1039/c3nr01574b

‡ These authors contribute equally to this paper.

increased with the La/Si molar ratio.¹⁸ Recently, we prepared a series of lanthanum functionalised nanoporous materials (La-SBA-15, La-FDU-12 and La-MOSF) *via* a wet impregnation method and studied their phosphate adsorption performances.^{21–23} It is demonstrated that the nucleation and growth of LaPO₄ can be controlled inside the porous channels/cages using adsorbents with sufficiently large pore diameters. However, the pores of mesoporous La-SBA-15 and La-FDU-12 can be blocked due to the growth of LaPO₄ nanocrystals inside the pores, thus limiting the La loading amount, the phosphate adsorption capacity and the La usage efficiency.^{21,22} The pore blocking phenomenon can be reduced by employing La-MOSF as the adsorbent with a macropore size larger than 50 nm,²³ thus the P removal efficiency can be further improved. It is noted that the aforementioned porous materials (MCM-41, SBA-15, FDU-12, and MOSF) are all prepared using surfactant templates, followed by a time-consuming and costly wet impregnation process. For industrial scale applications, there is a strong motivation to seek for alternative high performance adsorbents but with low production cost.

Herein, a facile spray-drying method has been developed for the large-scale fabrication of highly porous silica microspheres. Aerosil 200, a cheap and commercialised silica, is utilised as the sole precursor. No surfactant is required during the synthesis thus the cost is low. Moreover, lanthanum nitrate can be introduced *in situ* during spray drying and converted to lanthanum oxide by a post-calcination process. Thus, the undesired impregnation process can be avoided. Importantly, the resultant lanthanum functionalized microspheres have large pore sizes and high pore volumes, leading to excellent phosphate adsorption performance and fast kinetics at both high and low phosphate concentrations.

Experimental

Chemicals

All chemicals were used as received without further purification. Commercialized fumed silica Aerosil 200 was purchased from Degussa. Lanthanum nitrate (La(NO₃)₃·6H₂O), potassium dihydrogen orthophosphate (KH₂PO₄), and ascorbic acid were purchased from Merck. Ammonium molybdate ((NH₄)₂MoO₄) was from Ajax Finechem. Antimony potassium tartrate (K₂Sb₂(C₄H₂O₆)₂) was from Riedel-de Haen. Concentrated sulfuric acid (98 wt%) was from Sigma Aldrich. Distilled water was used for all experiments.

Preparation of spray dried Aerosil and lanthanum functionalised Aerosil

For the preparation of spray dried Aerosil 200 (A-SD), 1.2 g of Aerosil 200 (A) was dispersed in 100 mL of H₂O and then sonicated for 30 min. The resulting mixture was spray dried using a Buchi mini spray dryer B-290 at an inlet temperature of 220 °C, an aspirator rate of 100%, and a pump rate of 5% (1.5 mL min⁻¹). The as-synthesized sample was then calcined in air at 550 °C for 5 h.

For the preparation of lanthanum functionalised Aerosil (La_x-A, where *x* is the weight ratio percentage of La(NO₃)₃·6H₂O *versus* Aerosil 200), a different amount of La(NO₃)₃·6H₂O was introduced before the sonication, while other synthesis conditions were unchanged. For *x* = 100, 150, and 200, 1.2, 1.8, and 2.4 g of La(NO₃)₃·6H₂O was used, respectively. The yield of each synthesis is ~82% assuming that La(NO₃)₃·6H₂O is completely dehydrated to La(NO₃)₃ during spray drying. (The dehydration of La(NO₃)₃·6H₂O is completed at 180 °C, while the decomposition of La(NO₃)₃ begins at 250 °C.²⁴) In a typical experiment, 4.32 g of La₁₀₀-A can be obtained in the lab in 90 min.

Preparation of lanthanum functionalised Aerosil by the wet impregnation method

For comparison, lanthanum functionalised Aerosil 200 was also prepared by the wet impregnation method (*x* = 150). 1.8 g of La(NO₃)₃·6H₂O and 1.2 g of Aerosil 200 were dispersed in ethanol in a beaker sealed with a plastic lid. The mixture was stirred at 80 °C for 24 h. Then, the lid was taken off and the ethanol was evaporated completely. The as-synthesized sample was calcined in air at 550 °C for 5 h. This sample was denoted as La₁₅₀-A-WI.

Characterization

X-ray diffraction patterns were obtained on a Bruker D8 Advanced X-ray Diffractometer with Ni-filtered Cu Kα radiation at a voltage of 40 mV and a current of 30 mA. Transmission electron microscopy (TEM) experiments were conducted on an FEI Technai F30 operated at 300 kV. The samples for TEM were dispersed in ethanol, gently shaken, and then supported onto the copper grid. Elemental mapping was conducted on a JEOL JEM-2100 operated at 200 kV. Scanning electron microscopy (SEM) images were obtained on a JEOL JSM 7800 microscope operated at 5 kV. Energy dispersive spectroscopy (EDS) was carried out on a JEOL JSM-6460. The N₂ adsorption isotherms were measured at 77 K on a nitrogen adsorption apparatus (Tristar II) after degassing the samples at 200 °C for 24 h.

Phosphate adsorption

KH₂PO₄ was chosen as the phosphate source. 50 mg of adsorbent was dispersed in a centrifuge tube containing 50 mL of phosphate solution with different concentrations (ranging from 10–120 mg L⁻¹). All samples were placed in a rotary shaker at 298 K for 24 h. The shaking speed was kept at 150 rpm. The suspension was then centrifuged. The phosphate concentration of the supernatant was analysed by an M5 Multimode Microplate Reader (USA) using the standard ascorbic acid method.

All adsorption isotherms were fitted with the Freundlich isotherm model. The function is expressed as:

$$q_{\text{eq}} = KC_{\text{eq}}^{1/n}$$

where q_{eq} is the amount adsorbed at equilibrium (mmol g⁻¹), C_{eq} is the equilibrium solute concentration (mmol L⁻¹), K (mmol^(1-*n*) L^{*n*} g⁻¹) and *n* are empirical constants.

The kinetic study was carried out by dispersing 50 mg of adsorbent into 50 mL of 50 mg L⁻¹ phosphate solution. The suspensions were centrifuged immediately at a given time ($t = 30, 60, 120, 240, 480, 1080, \text{ and } 1440 \text{ min}$) for phosphate concentration analysis. The kinetic data for La₁₅₀-A were fitted to a pseudo second-order kinetic model, which can be expressed as:

$$\frac{dq_t}{dt} = k(q_{eq} - q_t)^2$$

where q_{eq} is the adsorption capacity at equilibrium (mmol g⁻¹), q_t is the amount adsorbed at a given t (mmol g⁻¹), and k is the rate constant (g mmol⁻¹ min⁻¹). Non-linear least squares regression analysis was applied to acquire the best estimation of all constants for all the models in the phosphate adsorption test.

The effect of pH on phosphate uptake capacity was studied by adjusting the pH value of the initial phosphate solution to the desired values, using 1 M NaOH or 0.1 M HCl solutions.

The effect of competing anions on phosphate adsorption capacity was studied in the presence of NaF, Na₂SO₄, NaCl, Na₂CO₃ or NaNO₃ with a concentration of 400 mg L⁻¹. The

phosphate concentration was fixed at 50 mg L⁻¹. The adsorbent (La₁₅₀-A) dosage was 50 mg per 50 mL.

Results and discussion

Porous silica microspheres were synthesized by the spray drying method using Aerosil 200 as the sole precursor. Aerosil 200 is a commercialised hydrophilic fumed silica. TEM characterization clearly shows that the primary nanoparticles have a typical size of 12 nm and interconnect with each other, forming highly branched agglomerates (Fig. 1a). After spray drying and the subsequent calcination, the Aerosil 200 nanoparticles are assembled into microspherical granules (denoted A-SD) with sizes of 1–5 μm as shown in SEM (Fig. 1b and c) and TEM images (Fig. 1d). Due to the highly branched nature of the agglomerates, the Aerosil 200 nanoparticles are not densely packed inside the A-SD microspheres. Instead, large interparticle voids can be directly observed by SEM (Fig. 1c). The highly porous characteristic of A-SD can be further confirmed by nitrogen adsorption results (Fig. 1e and f). As shown in Fig. 1e,

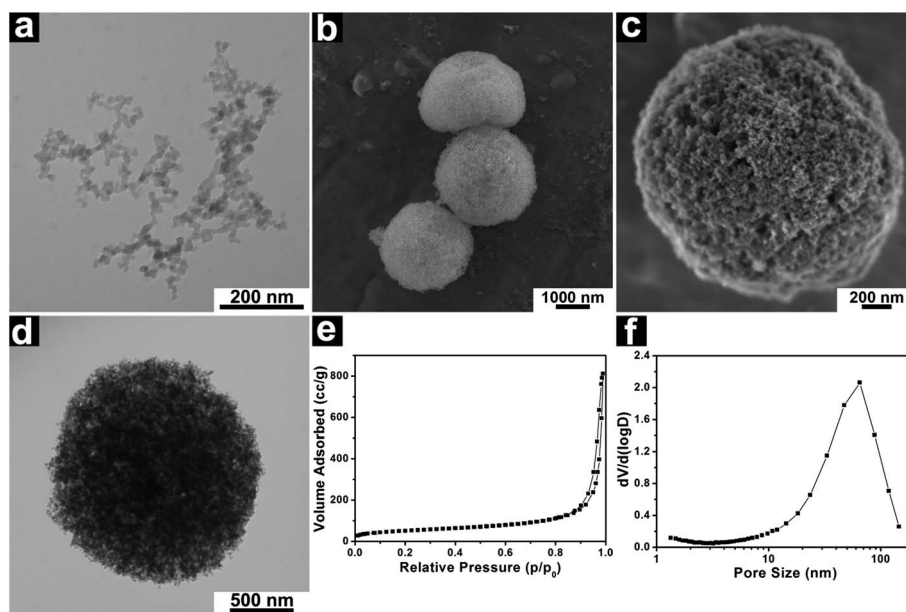


Fig. 1 TEM image of Aerosil 200 (a), SEM (b and c), TEM (d), N₂ adsorption-desorption isotherm (e), and pore size distribution of A-SD (f).

Table 1 Summarized properties of the adsorbents

Samples	S_{BET} (m ² g ⁻¹)	V (cm ³ g ⁻¹)	Pore size (nm)	Q_{max} (mmol g ⁻¹)	P/La	Freundlich model			La : Si (feed)	La : Si (EDX)
						K (mmol ⁽¹⁻ⁿ⁾ L ⁿ g ⁻¹)	n	R^2		
A	192	0.48	45	—	—	—	—	—	—	—
A-SD	180	1.26	70	—	—	—	—	—	—	—
La ₁₀₀ -A	90	0.81	64	1.946	1.160	1.198	8.519	0.999	1 : 4.94	1 : 4.89
La ₁₅₀ -A	87	0.53	48	2.317	1.003	1.266	6.405	0.998	1 : 3.3	1 : 3.52
La ₁₅₀ -A-WI	92	0.54	50	1.746	0.756	0.603	3.934	0.999	1 : 3.3	1 : 3.42
La ₂₀₀ -A	72	0.40	48	2.243	0.852	1.182	6.117	0.999	1 : 2.47	1 : 2.96
La ₂₀₀ MOSF ²³	172	0.92	100	2.272	0.862	1.831	3.177	0.973	1 : 2.47	1 : 4

A-SD shows a typical type II isotherm with a narrow H1 hysteresis loop at the high relative pressure (P/P_0) region. Accordingly, a broad pore size distribution centred at 65 nm can be found in Fig. 1f. Compared to Aerosil 200 (A), the A-SD shows a slightly reduced BET surface area (180 vs. 192 m² g⁻¹, see Table 1) due to the high temperature (550 °C) calcination treatment, but greatly enhanced pore volume (1.26 vs. 0.48 cm³ g⁻¹) due to the formation of ~65 nm nanopores after the spray drying process.

It is well-known that lanthanum species can bind to phosphate ions strongly, forming LaPO₄ with very low solubility. To functionalise the porous silica microspheres as a phosphate adsorbent, lanthanum nitrate was introduced *in situ* during spray drying. The morphology and structure of the La_x-A materials were characterized by SEM and TEM. Both SEM and TEM images demonstrate a microspherical morphology (Fig. 2a–g), similar to that of A-SD. The sizes of the microspheres are approximately 1–5 μm. Moreover, large inter-particle voids can also be observed in La_x-A (more clear in Fig. 2d). To show the advantage of spray drying, lanthanum functionalised Aerosil 200 (La₁₅₀-A-WI) was also prepared by the wet impregnation method. Under TEM observation (Fig. 2h), it is found that La₁₅₀-A-WI shows a similar morphology to untreated Aerosil 200. The composition of La_x-A and La₁₅₀-A-WI was studied by EDS (see ESI, Fig. S1†). As summarised in Table 1, the La : Si ratio of La_x-A and La₁₅₀-A-WI are close to their feed ratio.

The structure of all materials has been characterized by XRD (Fig. 3). A-SD shows a broad diffraction peak centred at ~22°, which is characteristic of amorphous silica.²⁵ With the introduction of lanthanum species with increasing amounts, the peak for amorphous silica weakens, and finally disappears. At the same time, two new broad peaks centred at 28° and 45° appear. The new broad diffraction peaks may be assigned to amorphous La₂O₃. The absence of any sharp diffraction peaks indicates a homogeneous distribution of amorphous or nano-sized La₂O₃ in the silica framework. In contrast to La_x-A, the product obtained by direct calcination of lanthanum nitrate at

550 °C is composed of highly crystalline La(OH)₃ (PDF no. 83-2034) and La₂O₂CO₃ (PDF no. 84-1963) (Fig. S2†).

Nitrogen adsorption analysis provides detailed textural properties of the products. The nitrogen adsorption–desorption isotherms and the corresponding BJH pore size distributions of La_x-A are shown in Fig. 4. The BET surface areas, pore sizes, and pore volumes are summarized in Table 1. Similar to A-SD, all La_x-A samples exhibit a type II isotherm and a H1 hysteresis loop (Fig. 4). The capillary condensation occurs at relatively high pressure ($P/P_0 > 0.9$), indicating the existence of macropores or large mesopores. According to our previous study, such large mesopores and macropores are advantageous over small mesopores with pore sizes less than 10 nm in phosphate adsorption.^{21–23} With the increase of La content (x) from 0 to 200, the change in pore size is not obvious; however, the pore

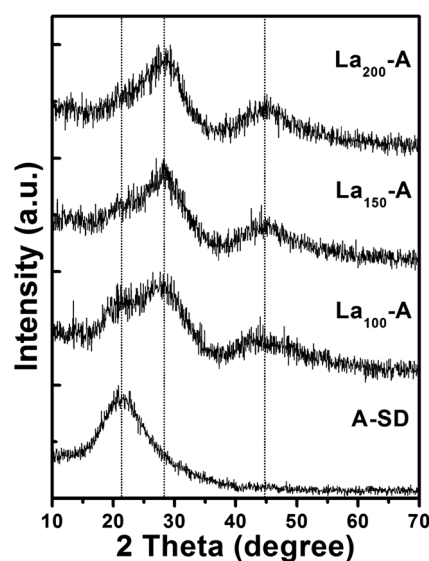


Fig. 3 XRD patterns of A-SD, La₁₀₀-A, La₁₅₀-A, and La₂₀₀-A.

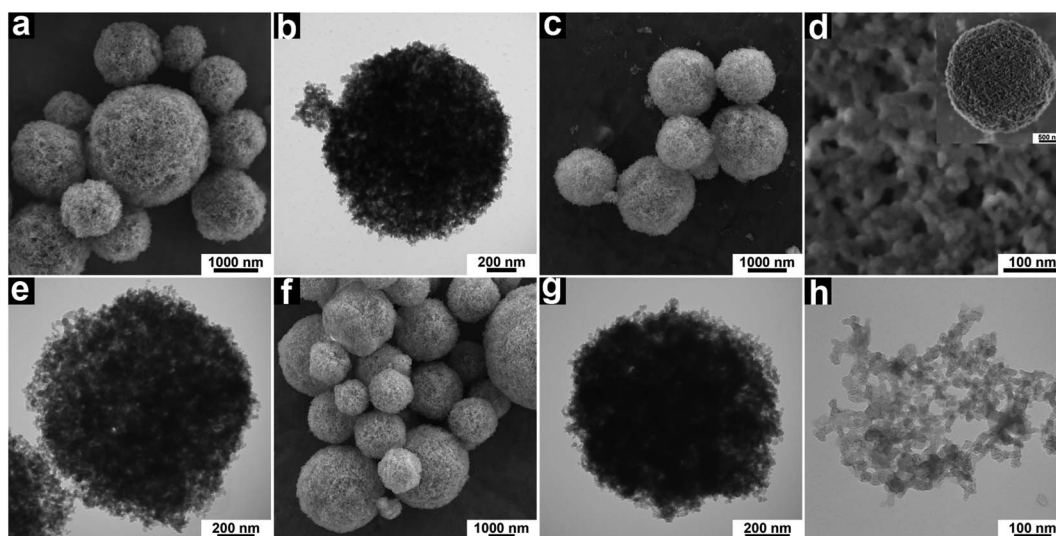


Fig. 2 SEM and TEM images of La₁₀₀-A (a and b), La₁₅₀-A, (c–e), La₂₀₀-A (f and g), and La₁₅₀-A-WI (h).

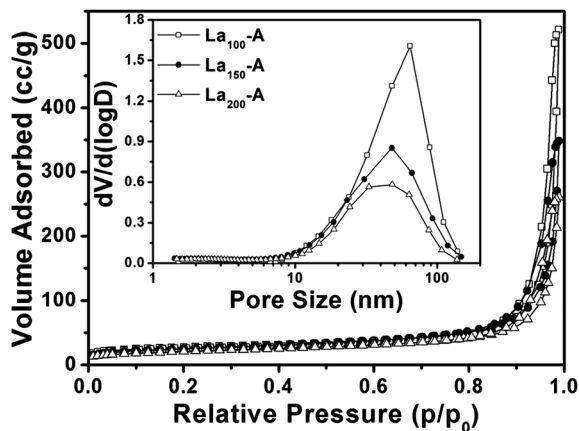


Fig. 4 Nitrogen adsorption-desorption isotherms and the corresponding BJH pore size distributions (inset) of $\text{La}_x\text{-A}$.

volume decreases dramatically from 1.26 to 0.40 $\text{cm}^3 \text{g}^{-1}$ and the BET surface area decreases from 180 to 72 $\text{m}^2 \text{g}^{-1}$. The reduction of surface area and pore volume can be attributed to the incorporation of high-density La_2O_3 (6.5 g cm^{-3}) within the low-density SiO_2 matrix (2.2 g cm^{-3}).

In order to determine the maximum phosphate adsorption capacity (Q_{max}) of $\text{La}_x\text{-A}$ and $\text{La}_{150}\text{-A-WI}$, the adsorption isotherms were measured at different concentrations of phosphate (Fig. 5 and Table 1). All the adsorption isotherm data can be well fitted to the Freundlich model with high correlation coefficients ($R^2 = 0.999$), indicating that the adsorption of phosphate ions is taking place in a multilayer adsorption fashion.²⁶ It is generally accepted that a value of $2 < n < 10$ represents easy adsorption, a value of $1 < n < 2$ represents somewhat difficult adsorption, and a value of $n < 1$ represents quite difficult adsorption. For all the $\text{La}_x\text{-A}$ materials, n falls between 2 and 10, suggesting that the phosphate anions can be easily adsorbed. Within our experimental range, the maximum phosphate adsorption capacity for $\text{La}_{100}\text{-A}$, $\text{La}_{150}\text{-A}$ and $\text{La}_{200}\text{-A}$ is 1.946, 2.317 and 2.242 mmol g^{-1} , respectively. For the lanthanum usage efficiency (P/La), it decreases continuously with the increase of lanthanum content (x), probably due to the gradually increasing

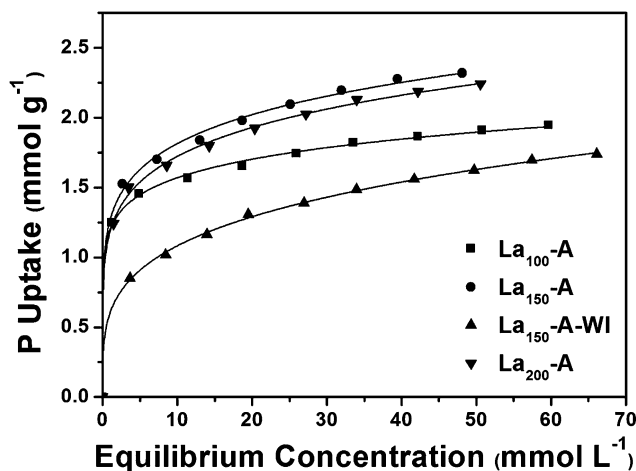


Fig. 5 Phosphate adsorption isotherm for $\text{La}_x\text{-A}$ and $\text{La}_{150}\text{-A-WI}$ materials.

size of lanthanum oxide in the composite. For $\text{La}_{100}\text{-A}$ and $\text{La}_{150}\text{-A}$, a lanthanum usage efficiency exceeding 1.0 is obtained, indicating the complete use of lanthanum for phosphate adsorption. While for $\text{La}_{200}\text{-A}$, a relatively low lanthanum usage efficiency of 0.852 is obtained. Due to the low lanthanum usage efficiency, the adsorption capacity of $\text{La}_{200}\text{-A}$ is even lower than that of $\text{La}_{150}\text{-A}$.

$\text{La}_{150}\text{-A}$ and $\text{La}_{150}\text{-A-WI}$ possess a similar BET surface area (87 and 92 $\text{m}^2 \text{g}^{-1}$) and pore volume (0.53 and 0.54 $\text{cm}^3 \text{g}^{-1}$). Unlike $\text{La}_{150}\text{-A}$ with a micron-sized spherical morphology, $\text{La}_{150}\text{-A-WI}$ has a structure similar to that of pristine Aerosil 200 and is fluffy, making it difficult to be handled in practice. Moreover, $\text{La}_{150}\text{-A}$ shows a much higher phosphate adsorption capacity compared to $\text{La}_{150}\text{-A-WI}$ (2.317 vs. 1.746 mmol g^{-1}) and La usage efficiency (1.003 vs. 0.756). It is concluded that the spray drying is advantageous over the impregnation method to prepare phosphate adsorbents with better performance while through a more convenient process.

Besides Q_{max} and P/La, the adsorption kinetics is another important aspect for an adsorbent. Thus, the phosphate adsorption kinetics of $\text{La}_{150}\text{-A}$, the material with the highest adsorption capacity, was further evaluated (Fig. 6). The experimental data fitted well with the pseudo-second-order kinetic model with a high correlation coefficient ($R^2 = 0.999$), suggesting that the adsorption occurs through chemisorption. The equilibrium was reached after

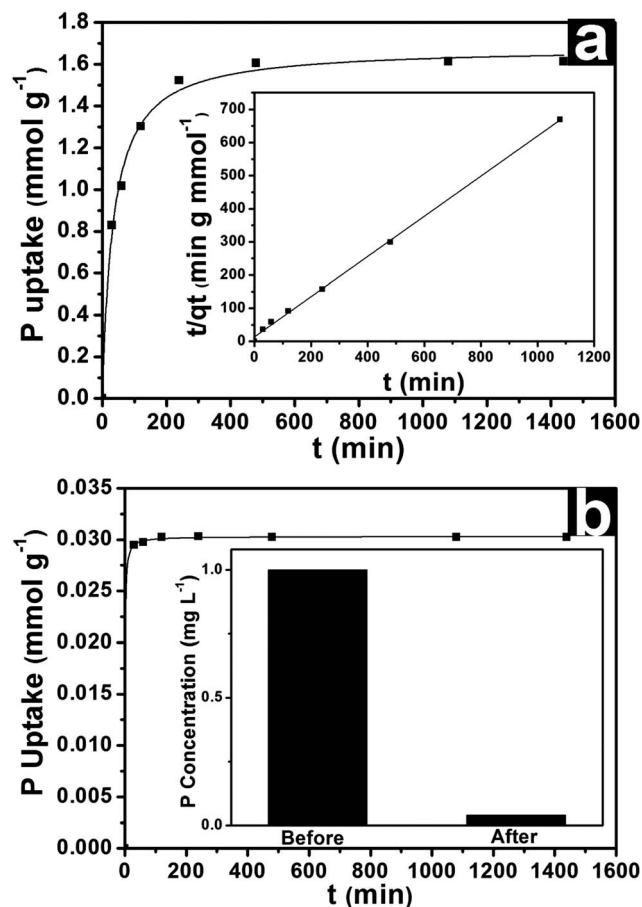


Fig. 6 Kinetic study of $\text{La}_{150}\text{-A}$ at a phosphate concentration of 50 mg L^{-1} (a), and 1 mg L^{-1} (b).

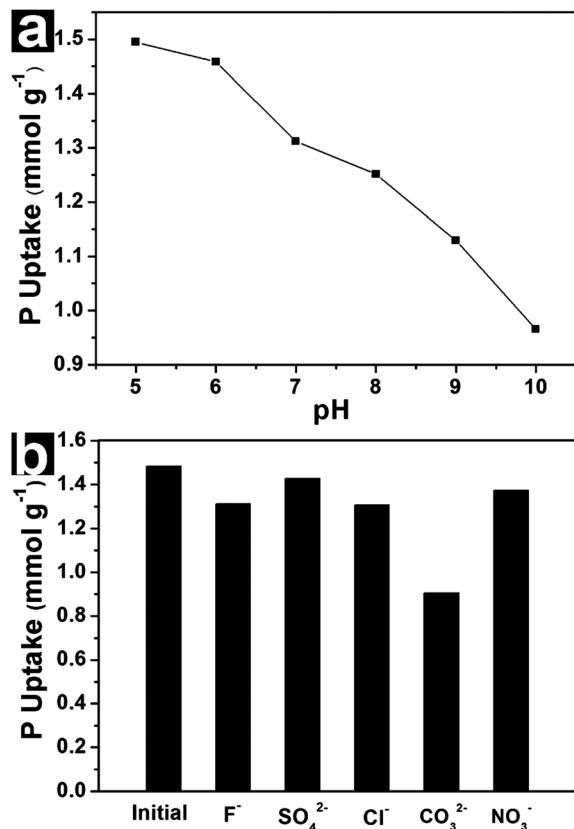


Fig. 7 Effect of pH (a) and competing anions (b) on phosphate adsorption performance of La₁₅₀-A.

~200 min. The rate constant (k), which represents the phosphate removal rate from the solution, is calculated to be 0.027 g mmol⁻¹ min⁻¹ (Fig. 6a, inset). This value is higher than that of La₂₀₀MOSF,²³ indicating the fast phosphate removal kinetics of La₁₅₀-A.

The adsorption performance at low phosphate concentration is of significant importance since a phosphate concentration as low as 1 mg L⁻¹ may also cause eutrophication.²⁷ Thus, the adsorption performance of La₁₅₀-A at a low phosphate concentration of 1 mg L⁻¹ was also studied (Fig. 6b). After adsorption for 24 h, the phosphate concentration drops from 1 to 0.06 mg L⁻¹ (Fig. 6b, inset), indicating that 94% of phosphate ions have been removed. In the kinetic study, the experiment data can be well fitted to the pseudo-second-order kinetic model ($R^2 = 0.999$) with a rate constant (k) of 37.65 g mmol⁻¹ min⁻¹. This value is twice higher than that of La₂₀₀MOSF reported previously,²³ suggesting the fast phosphate adsorption rate of La₁₅₀-A at such a low concentration.

The pH conditions of the water bodies may have an impact on the phosphate adsorption performance. Thus, the effect of pH on phosphate adsorption capacity of La₁₅₀-A was investigated by varying the initial pH value of the solution between 5.0 and 10.0 (Fig. 7a). The adsorbent dosage is 50 mg in 50 mL of phosphate solution, and the initial phosphate concentration was kept at 50 mg L⁻¹. As can be seen from Fig. 7a, with the increase of the pH value from 5 to 10, the adsorption capacity of La₁₅₀-A decreases from 1.49 to 0.96 mmol g⁻¹ (by 35.4%). Two possible reasons might be responsible for this phenomenon. First, the hydroxyl anions may compete with the phosphate ions for binding to the active sites of the adsorbent. Second, higher pH values may lead to more negative charges on the surface of the adsorbent, thus stronger electrostatic repulsion between the adsorbent and the phosphate ions.

Natural and industrial wastewater normally contains various anions, which may also bind to the adsorbent. The effects of coexisting anions on the adsorption performance of La₁₅₀-A were further evaluated. In the presence of 400 mg L⁻¹ of fluoride, sulfate, chloride, carbonate, and nitrate, the phosphate adsorption capacity of La₁₅₀-A is suppressed by 11.5%, 7.4%, 11.9%, 3.7% and 39.0%, respectively (Fig. 7b). The phosphate adsorption

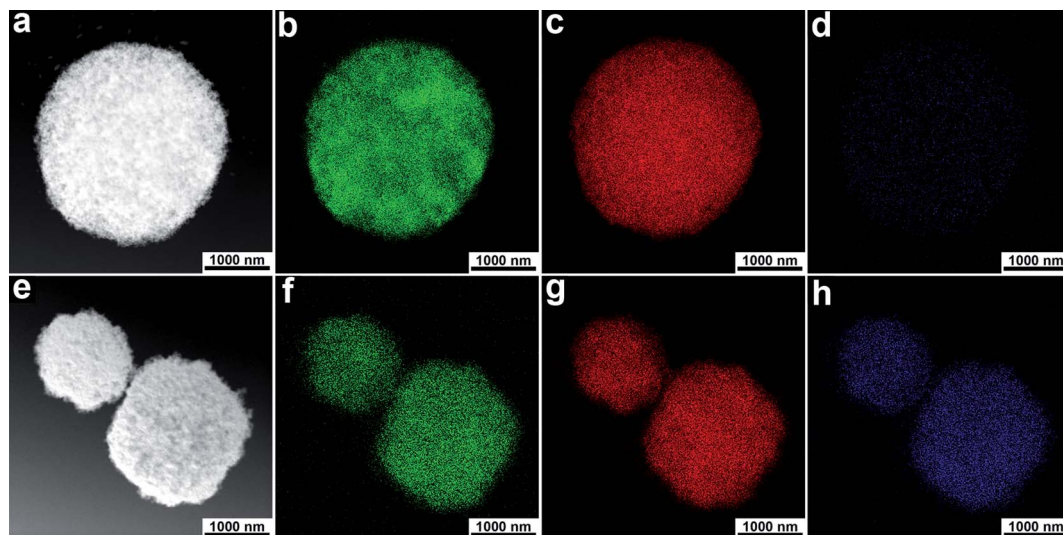


Fig. 8 HAADF-STEM images of La₁₅₀-A before and after phosphate adsorption. La (b and f), Si (c and g) and P (d and h) elemental maps of La₁₅₀-A before (b–d) and after (f–h) phosphate adsorption.

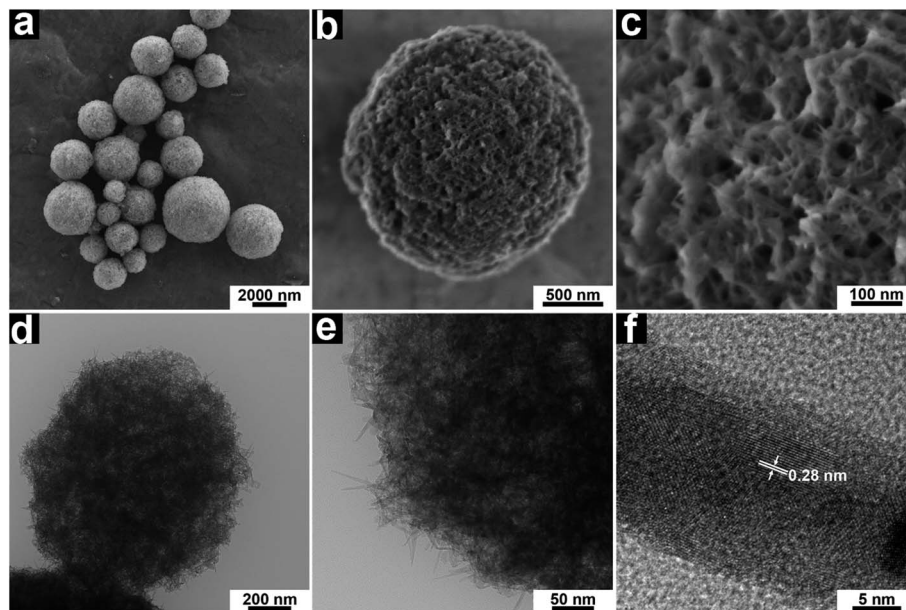


Fig. 9 SEM and TEM images of La₁₅₀-A after 24 h of phosphate adsorption at 50 mg L⁻¹.

capacity is more affected by carbonate ions due to the low K_{sp} of La₂(CO₃)₃ (3.98×10^{-34}).

In order to understand the phosphate adsorption mechanism, the La₁₅₀-A adsorbent after phosphate adsorption was carefully characterized. Fig. 8 shows the elemental maps of La₁₅₀-A before and after P adsorption. Before adsorption, it is observed that the La element is distributed homogeneously in the whole silica framework (Fig. 8a–c); no P element can be detected (Fig. 8d). After adsorption, the homogeneous distribution of P element in the entire microsphere can be detected (Fig. 8e–h), suggesting that the phosphate ions have been trapped by the adsorbent. The XRD pattern of the La₁₅₀-A material after 24 h of phosphate adsorption is shown in Fig. S3.† The diffractions can be predominantly indexed as a hexagonal LaPO₄ phase with cell parameters of $a = 0.7081$ and $c = 0.6468$ nm (PDF no. 75-1881). The diffraction peaks are relatively broad, indicating the nanocrystalline nature of LaPO₄.

Fig. 9 shows the SEM and TEM images of La₁₅₀-A after 24 h of phosphate adsorption. The microspherical morphology can be well preserved during adsorption (Fig. 9a and b). Besides the microspheres, no other particles can be found. Under higher magnifications (Fig. 9c), one may find that the surface of the microspheres is fully covered with nanorods with diameters of ~10 to 20 nm. TEM characterization further confirms the existence of rod-like nanocrystals on the surface and probably inside the microspheres (Fig. 9d and e). The high resolution TEM (HRTEM) image demonstrates that the nanorods are hexagonal LaPO₄; the (102) inter-planar spacing (0.28 nm) of LaPO₄ can be clearly distinguished (Fig. 9f).

Based on the elemental mapping, XRD, and TEM results, it is concluded that after spray drying and calcination treatment, amorphous La₂O₃ is distributed homogeneously inside the porous matrix of La₁₅₀-A microspheres. This feature, together with the large nanopores and high pore volumes, leads to fast

adsorption of phosphate ions bound to the active sites and eventually growth of LaPO₄ nanocrystals confined within the La₁₅₀-A microspheres.

Conclusions

In summary, this work has the following contributions to a broad field of materials science. Firstly, a facile spray drying method has been developed for large-scale and template-free production of nanoporous silica with controlled morphology, large pore size, high pore volume, and cheap prices. Secondly, it is demonstrated that this approach can be extended to the preparation of functional nanoporous materials, in this study, lanthanum oxide functionalised silica microspheres. Owing to the controlled nanostructures, the resultant La_x-A materials exhibit high phosphate adsorption capacity, fast kinetics, and excellent adsorption performance at low phosphate concentration, even better than previous reports where expensive nanoporous materials were utilised as the host materials. In virtue of the easy and scalable synthesis, low cost, and excellent phosphate adsorption performances, the La_x-A materials might have a bright future in wastewater treatment. It is expected that our approach is not limited only to lanthanum functionalisation. More functionalised porous materials with low-cost and high performance will be fabricated following the success of this work, significantly advancing the research field of nanoporous materials.

Acknowledgements

We thank the Australian Research Council for financial support. We acknowledge the facilities, and the scientific and technical assistance, of the Australian Microscopy & Microanalysis Research Facility at the Centre for Microscopy and

Microanalysis, The University of Queensland. We would like to thank Ms Anya Yago from the Centre of Microscopy and Microanalysis for the XRD measurement. We thank Mr Hongyi Xu and Prof. Jin Zou for the help in SEM. We greatly thank Degussa company for their kindness in providing the Aerosil200 sample.

References

- 1 M. E. Davis, *Nature*, 2002, **417**, 813.
- 2 C. T. Kresge, M. E. Leonowicz, W. J. Roth, J. C. Vartuli and J. S. Beck, *Nature*, 1992, **359**, 710.
- 3 D. Y. Zhao, J. L. Feng, Q. S. Huo, N. Melosh, G. H. Fredrickson, B. F. Chmelka and G. D. Stucky, *Science*, 1998, **279**, 548.
- 4 H. N. Wang, X. F. Zhou, M. H. Yu, Y. H. Wang, L. Han, J. Zhang, P. Yuan, G. Auchterlonie, J. Zou and C. Z. Yu, *J. Am. Chem. Soc.*, 2006, **128**, 15992.
- 5 A. Imhof and D. J. Pine, *Nature*, 1997, **389**, 948.
- 6 O. D. Velev, T. A. Jede, R. F. Lobo and A. M. Lenhoff, *Nature*, 1997, **389**, 447.
- 7 T. Yokoi, Y. Sakamoto, O. Terasaki, Y. Kubota, T. Okubo and T. Tatsumi, *J. Am. Chem. Soc.*, 2006, **128**, 13664.
- 8 J. W. Tang, X. F. Zhou, D. Y. Zhao, G. Q. Lu, J. Zou and C. Z. Yu, *J. Am. Chem. Soc.*, 2007, **129**, 9044.
- 9 T. Ishimori and M. Senna, *J. Mater. Sci.*, 1995, **30**, 488.
- 10 A. Maskara and D. M. Smith, *J. Am. Ceram. Soc.*, 1997, **80**, 1715.
- 11 F. Iskandar, I. W. Lenggoro, B. Xia and K. Okuyama, *J. Nanopart. Res.*, 2001, **3**, 263.
- 12 D. J. Conley, H. W. Paerl, R. W. Howarth, D. F. Boesch, S. P. Seitzinger, K. E. Havens, C. Lancelot and G. E. Likens, *Science*, 2009, **323**, 1014.
- 13 S. R. Carpenter, *Proc. Natl. Acad. Sci. U. S. A.*, 2008, **105**, 11039.
- 14 D. W. Schindler, R. E. Hecky, D. L. Findlay, M. P. Stainton, B. R. Parker, M. J. Paterson, K. G. Beaty, M. Lyng and S. E. M. Kasian, *Proc. Natl. Acad. Sci. U. S. A.*, 2008, **105**, 11254.
- 15 X. Cheng, X. R. Huang, X. Z. Wang, B. Q. Zhao, A. Y. Chen and D. Z. Sun, *J. Hazard. Mater.*, 2009, **169**, 958.
- 16 D. Y. Zhao and A. K. Sengupta, *Water Res.*, 1998, **32**, 1613.
- 17 E. W. Shin, J. S. Han, M. Jang, S. H. Min, J. K. Park and R. M. Rowell, *Environ. Sci. Technol.*, 2004, **38**, 912.
- 18 E. Ou, Z. J. Junjie, M. C. Shaochun, W. Q. Jiaqiang, X. Fei and M. Liang, *Colloids Surf., A*, 2007, **308**, 47.
- 19 P. Delaney, C. McManamon, J. P. Hanrahan, M. P. Copley, J. D. Holmes and M. A. Morris, *J. Hazard. Mater.*, 2011, **185**, 382.
- 20 J. D. Zhang, Z. M. Shen, W. P. Shan, Z. Y. Chen, Z. J. Mei, Y. M. Lei and W. H. Wang, *J. Environ. Sci.*, 2010, **22**, 507.
- 21 J. Yang, L. Zhou, L. Z. Zhao, H. W. Zhang, J. N. Yin, G. F. Wei, K. Qian, Y. H. Wang and C. Z. Yu, *J. Mater. Chem.*, 2011, **21**, 2489.
- 22 J. Yang, L. Zhou, J. Zhang, J. Zou, Z. G. Yuan and C. Z. Yu, *Chem.-Eur. J.*, 2013, **19**, 5578.
- 23 J. Yang, P. Yuan, H. Y. Chen, J. Zou, Z. G. Yuan and C. Z. Yu, *J. Mater. Chem.*, 2012, **22**, 9983.
- 24 S. Mentus, D. Jelic and V. Grudic, *J. Therm. Anal. Calorim.*, 2007, **90**, 393.
- 25 H. G. Zhu, B. Lee, S. Dai and S. H. Overbury, *Langmuir*, 2003, **19**, 3974.
- 26 N. Ping, H. J. Bart, L. Bing, X. W. Lu and Y. Zhang, *J. Environ. Sci.*, 2008, **20**, 670.
- 27 X. Huang, X. P. Liao and B. Shi, *J. Hazard. Mater.*, 2009, **166**, 1261.